Temperature profiles from two close lidars and a satellite to infer the structure of a dominant gravity wave

P. Alexander[1], A. de la Torre[2], N. Kaifler[3], B. Kaifler[3], J. Salvador [4,5], P. Llamedo[2], R. Hierro[2]and J. L. Hormaechea [6]

[1]Instituto de Física de Buenos Aires, CONICET, Ciudad Universitaria Pabellón 1, 1428 Buenos Aires, Argentina

[2]LIDTUA, Facultad de Ingeniería, Universidad Austral and CONICET, 1629 Pilar, Provincia de Buenos Aires, Argentina

[3]Institute of Atmospheric Physics, German Aerospace Center, Oberpfaffenhofen, Germany

[4]Laser and Application Research Center (CEILAP) –UNIDEF (MINDEF –CONICET), Villa Martelli, Argentina

[5]Instituto de Tecnología Aplicada, Universidad Nacional de la Patagonia Austral, Unidad Académica Río Gallegos

[6]Estación Astronómica Río Grande, Facultad de Ciencias Astronómicas y Geofísicas, Universidad Nacional de La Plata and CONICET, Argentina

Key Points:

- The 3D reconstruction of gravity waves (GW) is a difficult task with present observational techniques
- The austral tip of South America is a well-known region of very intense GW, but their sources and effects are still unclear
- With two close lidars in the hotspot zone and a satellite profile, the full 3D wavevector and the intrinsic frequency of observed GW may be determined

Corresponding author: Peter Alexander, peter@df.uba.ar

This article has been accepted for publication and undergone full peer review but has not been through the copyediting, typesetting, pagination and proofreading process which may lead to differences between this version and the Version of Record. Please cite this article as doi: 10.1029/2020EA001074

Abstract

Gravity waves (GW) are a crucial coupling mechanism for the exchange of energy and momentum flux (MF) between the lower, middle and upper layers of the atmosphere. Among the remote instruments used to study them, there has been a continuous increment in the last years in the installation and use of lidars (light detection and ranging) all over the globe. Two of them, which are only night-operating, are located in Río Gallegos (-69.3W, -51.6S) and Río Grande (-67.8W, -53.8S), in the neighborhood of the austral tip of South America. This is a well-known GW hotspot from late autumn to early spring. Neither the source for this intense activity nor the extent of its effects have been yet fully elucidated. In the last years, different methods that combine diverse retrieval techniques have been presented in order to describe the three-dimensional (3D) structure of observed GW, their propagation direction, their energy and the MF that they carry. Assuming the presence of a dominant GW in the covered region, we develop here a technique that uses the temperature profiles from two simultaneously working close lidars to infer the vertical wavelength, ground-based frequency and horizontal wavelength along the direction joining both instruments. If in addition within the time and spatial frame of both lidars there is also a retrieval from a satellite like SABER (Sounding of the Atmosphere using Broadband Emission Radiometry), then we show that it is possible to infer also the second horizontal wavelength and therefore reproduce the full 3D GW structure. Our method becomes verified with an example that includes tests that corroborate that both lidars and the satellite are sampling the same GW. The improvement of the Río Gallegos lidar performance could lead in the future to the observation of a wealth of cases during the GW high-season. Between 8 and 14 hours (depending on the month) of continuous nighttime data could be obtained in the stratosphere and mesosphere in simultaneous soundings from both ground-based lidars.

1 Introduction

Gravity waves (GW) have significant global effects from the lower to the upper atmosphere [e.g., Gill, 1982; Fritts and Alexander, 2003]. They are mainly generated in the troposphere or stratosphere and may increase in amplitude under vertical propagation in certain conditions. These waves may transfer significant amounts of energy and momentum flux (MF) to the background if filtering or dissipation occurs while they propagate. This may result in strong forcing of the dynamics and thermal structure, mainly in the

middle atmosphere. Some works have shown that GW may even penetrate and influence the thermosphere and ionosphere [e.g., Park et al., 2014; P. Alexander et al., 2015].

Although the austral tip of South America may be the most intense hotspot of GW on the globe from austral late autumn to early spring [e.g., Ern et al., 2004; P. Alexander et al., 2010; Hoffmann et al., 2013, 2016], several studies using lidars (light detection and ranging), aircrafts, radars or balloons have focused on the Northern Hemisphere (NH). However, in the last years there has been a growing awareness of the relevance of this GW hotspot close to the Southern pole [e.g., Kaifler et al., 2015; Fritts et al., 2016; Zhao et al., 2017; Chu et al., 2018; Llamedo et al., 2019]. The importance of an improvement in the knowledge of this region is highlighted by the fact that comparisons of stratospheric GW MF obtained from general circulation models (GCM) and satellite data reveal some notable discrepancies. Although there are some well reproduced features, large deviations are still present [e.g., Geller et al., 2013; de la Cámara et al., 2016]. For example, several GCM produce simulations of the Southern Hemisphere (SH) polar stratosphere that lead to significant underestimations of the temperatures and drag on the winds [e.g., Butchart et al., 2011; Wright and Hindley, 2018]. Numerical solutions are not able to resolve the full spectrum of waves. Parameterizations of the smallest scale GW are then introduced but they are usually too coarse and may be a major cause of the biases in the polar SH stratospheric dynamics and thermal structure simulations [McLandress et al., 2012]. These shortages recall the need for observational information on GW sources, evolution and general behavior in this zone. The possible but still uncertain causes of the intense GW activity are usually attributed to orography (Southern Andes, Antarctic Peninsula or small oceanic islands), non-orographic waves from winter storm tracks over the Southern oceans or from spontaneous adjustment or jet instability around the edge of the stratospheric vortex or secondary waves stemming from primary breaking ones from any source [e.g., Sato et al., 2009; M.J. Alexander and Grimsdell, 2013; Hindley et al., 2015].

The DIAL (Differential Absorption Lidar) instrument, belonging to the Centro de Investigaciones en Láseres y Aplicaciones (CEILAP) was located in 2005 at the Observatorio Atmosférico de la Patagonia Austral (OAPA) in Río Gallegos (51.6S, 69.3W), mainly for ozone studies. This lidar was the southernmost to the North of Antarctica until November 2017, when CORAL (Compact Rayleigh Autonomous Lidar) started working in Río Grande (53.8S, 67.8W). Río Gallegos is nearly 300 km to the East of the Andes and 70 km to the North of the Strait of Magellan, whereas Río Grande is further Southeast

on the Atlantic coast of the Tierra del Fuego island (Figure 1). Both are in an excellent position in relation to the observation of the GW hotspot and are separated by 265.6 km (zonal and meridional distances of 100.8 km and 245.7 km).

It is not possible to determine the MF of a dominant GW and its 3D structure with the temperature retrieval from one lidar. However, it may be feasible to obtain additional information with a second simultaneous and close lidar through the phase shift between GW induced perturbations on both soundings and the knowledge of the spatial separation of both instruments. If in addition there is another close temperature profile, for example provided by a satellite, then it may be possible to reveal the full 3D GW structure, including the net MF calculation. The satellite measurements like those from SABER (Sounding of the Atmosphere using Broadband Emission Radiometry), GPS radio occultation or HIRDLS (High Resolution Dynamics Limb Sounder) provide no directional information of the horizontal components of the momentum flux vector, but only the absolute value of each one can be found. However, an inspection of the horizontal components of the equation of motion for the atmosphere shows that the net momentum fluxes affect the wind and temperature structure [e.g., Geller et al., 2013]. Wright et al. [2016] also remarked the importance of obtaining the net rather than the absolute value. In brief, we suggest to use a sequence of vertical temperature profile pairs over a time interval plus a static retrieval. As far as we know, there have been no previous similar studies. Just frozen GW reconstructions have been usually obtained from a combination of instantaneous satellite temperature profiles which are close in space and time [e.g., Ern et al., 2004; Schmidt et al., 2016; Ern et al., 2017; P. Alexander et al., 2018], as the evolution could not be monitored in those cases.

In the present study we employ a set of two close and simultaneous lidar temperature measurements over time and height and a third instantaneous retrieval from a satellite within the same spatial and time frame in order to infer the ground-based frequency and the three cartesian wavelengths of a dominant GW in the studied zone. This also allows the determination of the 3 phase velocity components and the net GW MF. Section 2 explains the analysis procedure here employed and the general characteristics of the data from both lidars and from the SABER instrument onboard the TIMED (Thermosphere Ionosphere Mesosphere Energetics Dynamics) satellite that we use in an application example in Section 3. Section 4 summarizes the constraints of the method and the main results of our case study.

2 Data and Method

The DIAL lidar at Río Gallegos has four Newtonian telescopes of 0.5 m diameter. Four Rayleigh and two Raman digital channels record the backscattered photons emitted by the third harmonic of the Nd-YAG laser at 355 nm (130 mJ maximum energy) with a 30 Hz repetition rate. For details on DIAL working characteristics see Llamedo et al. [2019]. Above 30 km altitude, temperature T is obtained using the Rayleigh scattering technique, whereas below the method is affected by aerosol scattering and ozone absorption. The spatial / temporal resolution of the photon counting system is 15m / 1 min respectively, but an integration of at least 900m / 30 min is needed to improve the signal-to-noise ratio (SNR). A careful analysis revealed that a significant fraction of oscillations above 40 km height with a 30 min integration time may be caused by noise. Moreover, very large negative temperature gradients are unlikely to persist as they are convectively unstable. The DIAL signal power is about 4 W.

The CORAL lidar measures atmospheric backscatter profiles from 22 to 90 km altitude, but only values above 30 km should be used due to the effect of aerosols. It is a Nd:YAG laser generating 12 W at 532 nm and 100 Hz pulse repetition rate. The telescope comprises a 630 mm diameter f/2.45 parabolic mirror. At the top altitude, the T derivation procedure is seeded by SABER temperature. Retrievals with a temporal and vertical resolution of respectively up to 10 min and 0.3 km may be provided with reasonable SNR values. For a description of CORAL characteristics see Kaifler et al. [2017].

With the two lidars we may obtain a two-dimensional (2D) scenario over several hours. In order to be able to fully resolve the 3D structure of a GW observed by both lidars, an additional profile must be provided. SABER soundings [Mlynczak, 1997], if present within the time and space frame, seem to be a good option as they measure T roughly between 20 and 100 km height. Although this retrieval is instantaneous, it helps to resolve the 3D GW structure over the whole observational period of both lidars (assuming the wave persists and does not suffer a substantial modification during all that time). Here we use kinetic temperatures from version 2.0 datasets.

A first step requires the separation in all the T profiles of GW from the background, including planetary waves (PW) if present. In general, special care has to be taken in avoiding spurious amplifications of GW near the altitudes of sharp changes (tropopause or stratopause) when using a digital filter to isolate these waves [e.g., de la Torre et al.,

2006]. Due to the limited vertical range of reliable lidar data in Río Gallegos (30-40 km) we do not undergo that problem. We follow Ehard et al. [2015]; Rapp et al. [2018] in that at middle and high latitudes a digital filter cutoff at 15 km of vertical distance separates GW from PW. As we have a 10 km vertical interval of data, a bandpass between 2 and 10 km will respectively contemplate the Nyquist condition (a vertical resolution of 1 km and sampling of 100 m is used for consistency in both lidars) and the elimination of the background and PW. We used a Savitzky-Golay filter [Orfanidis, 1996]. Regarding the time evolution of both lidars we implemented for consistency intervals of 30 min. The same filter was used below for the SABER profile.

We assume that a dominant monochromatic GW is present at both lidars during the whole sounding period or at least a significant fraction of it. In the last case the different portion should be identified from the data. The perturbed temperature $T'_{A,R}$ respectively at Río Gallegos ($_A$) and Río Grande ($_R$) may be then represented by

$$T'_{A,R}(x, y, z, t) = T_o \sin(k x_{A,R} + l y_{A,R} + mz - \omega t + \varphi_0) \tag{1}$$

where x, y, z, t represent zonal, meridional and vertical coordinates and time, k, l, m, ω are the corresponding wavenumbers and frequency as seen from the ground, T_o is the GW amplitude (we consider it to be constant due to the limited height range), φ_0 is a fixed value, whereas on the right hand-side the expression within parentheses is the wave phase. If for both lidars we represent as usual T' against z and t, we should then get a similar ω and m if both places are observing the same dominant wave and are subject to similar mesoscale conditions. If so, it means we obtained the ground-based frequency and the vertical wavelength.

Between the two lidars at a fixed time and height the phase difference $d\phi_{AR}$ is given by

$$d\phi_{AR} = k(x_A - x_R) + l(y_A - y_R) \tag{2}$$

If we put the origin in Río Grande and rotate the horizontal cartesian coordinate system so that the y^* axis coincides with the direction to Río Gallegos (see Figure 1), then we may rewrite

$$d\phi_{AR} = l^*(y^*_A - y^*_R) \tag{3}$$

Equation (3) shows that if the phase difference is found, as the horizontal separation between both lidars is known it is possible to obtain the component of the horizontal wave vector defined by the direction that joins both places. To reconstruct the full 3D GW

structure, only one horizontal wavelength is missing. This information may be provided by an additional profile. To optimize its added value, its location in the horizontal plane should not lie along the y* axis (the new information would be redundant) but rather separated from it.

In addition, to ensure that it may be observing the same dominant GW we restrict its separation from any of both places to less than 2.5 ^{o} in latitude and 4 ^{o} in longitude (the angle difference keeps the maximum possible zonal and meridional separations equal). A minimum distance, e.g. 50 km, should be set to avoid uncertainties being larger than the possible small phase difference for a too close comparison. It will be shown below that the SABER horizontal excursion for measurements between 30 and 40 km height is small compared to the horizontal wavelength found in our example, so we essentially consider it a vertical profile. The second horizontal equation between SABER and Río Gallegos then is

$$d\phi_{SA} = k^*(x_S^* - x_A^*) + l^*(y_S^* - y_A^*) \tag{4}$$

where l^* was already found in Equation (3), the positions are known, so k^* can be calculated.

The determination of GW phase differences between both lidars as a function of height at consecutive 30 min intervals has been performed by wavelet coherence [Torrence and Compo, 1998]. We first assumed that $d\phi_{AR}$ was between $-\pi$ and π. However, we then also contemplated the 3 other possible aliased phase differences between -4π and 4π. This implies physically that we also contemplate waves with smaller wavelengths and/or propagating in the opposite direction than the initial one. Aliasing is not expected in the vertical direction or time, as it would imply wavelengths smaller than 2 km and ground-based periods of less than 1 h. We will then obtain 4 possible solutions. Once we derive the missing horizontal wavelength for each of the 4 aliased cases, the "true" value will be selected as the one that better suits the GW dispersion relation. It is given in terms of the intrinsic frequency $\hat{\omega}$ by

$$\hat{\omega}^2 = \frac{N^2 k_h^2 + f^2(m^2 + l/4H^2)}{k_h^2 + m^2 + l/4H^2} \tag{5}$$

where H is the scale height, $k_h^2 = k^2 + l^2 = k^{*2} + l^{*2}$ is the squared total horizontal wavelength, N is the Brunt-Väisälä frequency, which will be obtained from ERA Interim reanalysis T profiles adequately interpolated in time and space but may be also obtained from any lidar [Chu et al., 2018]. The reanalysis horizontal components of wind were

used in order to calculate the intrinsic frequency on the left hand-side ($\hat{\omega} = \omega - kU - lV$ with U and V the zonal and meridional projections of air velocity). A similar procedure to discard spurious aliased cases was already used by P. Alexander et al. [2018].

Fortunately the part of the year with the longest nights coincides with the months of the most intense GW. From March to October 2018 there were 17 coincident measurement periods of both lidars, ranging from 4 to 12 hours of simultaneous sounding intervals. The relatively low number of concurrent observations as compared to the total number of nights is due to cloudy conditions or to operational problems in any of both places. To make both datasets comparable, the information from Río Grande was restricted to the 30-40 km height interval, all the profiles were provided every 30 min and the vertical resolution was set to 1 km. The T retrievals were initially used from 27 to 42 km height, but after retaining the GW they were restricted to 30-40 km. This procedure was only done to attenuate any artificial discontinuity at the beginning or end of the dataset due to the implicit assumption of the digital filtering procedure that it is cyclic, which may introduce spurious temperature fluctuations [Ehard et al., 2015]. Although all the profiles already underwent quality control verifications, we tested them against anomalous temperature values (below 160 K or above 320 K).

After the 17 matrix pairs of T' against height (every 100 m in the 30-40 km range) and time (every 30 min along the coincident observational period) were obtained, different procedures were developed to ensure that both lidars detect the same GW and adequately. A minimum of 10 consecutive with up to 1 missing measurement (to be interpolated) time was requested. By visual inspection we kept only cases that exhibited the presence of wavefront-like features and eliminated cases with clearly identifiable noisy patterns in either lidar site, whereby 8 cases out of 17 passed this selection process. In every matrix pair we searched at every fixed time a dominant mode that was present and found its phase difference at both places by wavelet coherence [Torrence and Compo, 1998]. If $d\phi_{AR}$ had an abrupt change at any height (> 0.2 rad in 100 m), then the pair was discarded as it may mean that different phenomena were observed at both places. Or diffusion or absorption or any instability happened or simply the main observed effects cannot be explained in terms of a significant GW or its properties stayed beyond the observational window of the lidars (we recall that no instrument may capture the whole spectrum of waves). With these requirements only 4 nights from March to June were still suitable for further analysis.

For these remaining cases we applied 2D wavelet analysis to each $T'(t, z)$ matrix [Wang and Lu, 2010; Kaifler et al., 2017]. The spectral power (SP) as a function of height, time, vertical wavelength and period was obtained for each lidar and event, whereby the largest value indicated the dominant mode and location. In order to ensure that the main GW seen at each site was similar to the other one, we required that they both become represented by slightly differing elements of the 2D wavelets basis: the angle and magnitude that define the dominant mode for each lidar sounding should deviate by less than $\pi/10$ and by less than 10 units (as vertical spacing is 100 m this represents for example 1 km in the z direction). After this evaluation only two cases were found to meet these criteria. However, when requiring that the evaluation of Equation (5) should differ by less than 10% as calculated on both hand-sides only one event remained. Larger deviations could mean that we are not observing a GW or it may be undergoing non-linear behavior at any of both places. We show in the Appendix some characteristics of the case that missed our last test and give some remarks on its failure.

3 Application Example

The case to be analyzed is June 01, 2018 21:50 to June 02, 2018 10:08 (all times in UTC). In Figure 2 we show SP for both lidars. The outcome of the 2D Morlet wavelet is determined in terms of two parameters: the angle θ which defines the direction of the mode in $t - z$ space and the scale s, which is the wavelength along the angle direction. SP was initially obtained as a function of z, t, θ and s, whereby the summation over the former two variables yielded SP as a function of the latter two. Differences in angle and scale for the dominant mode in both lidars were respectively less than $\pi/20$ and 0.1 km and their values were $\pi/2$ and 5 km. Notice that $\theta = \pi/2$ implies stationary wavefronts, as they are represented by horizontal lines in the t, z plane. In Figure 3 we show the location of the polar vortex. To obtain it at different heights, we used ERA Interim data at 475, 600 and 700K isentropic levels to find the largest potential vorticity gradient weighted by the horizontal wind speed [Nash et al., 1996]. It can be seen that both lidars are outside and far away from the vortex, so direct effects on both soundings or the presence of non-stationary GW induced by geostrophic adjustment are unlikely. It should be mentioned that in some occasions the edge may reach or even surpass one or both sites. In addition, to analyze if all the studied region exhibits similar mesoscale features we show in Figure 4 the horizontal velocity at 600, 100 and 10 mb levels. Although the dominant wind direc-

tion changes with height, homogeneous conditions can be observed at every single altitude shown. We therefore expect uniform background characteristics in the whole observed zone. In addition, in the lower left part of the 600 mb panel (a level close to the height of the local Andes mountains), adequate conditions for the generation of mountain waves are observed. The prevailing wind finds a meridional obstacle, thus probably generating GW [Baines, 1995]. Moreover, the other panels show that at least at those two other heights critical levels for stationary mountain waves are unlikely (no zero wind regions).

In Figure 5 we show the T' representation against time and height for both lidars. Notice some general similarities regarding the nearly stationary wavefronts. The best fit wavefront maxima are also shown (i.e. the optimal phase for a 5 km vertical wavelength was searched in each case). In Figure 6 we show the SABER profile. We used the same bandpass filter between 2 and 10 km as with the lidar data. Notice a clear nearly 5 km vertical periodicity. The sounding was located about 334 km northeast from Río Gallegos, so the 50 km minimum distance requirement was fulfilled. Equation (4) was used to calculate the missing component k^*. The total horizontal wavelength that was found is 155 km and the deviation from the East direction was 2.2 ^{o} anticlockwise. The SABER horizontal displacement for measurements from 30 to 40 km height is 0.18 ^{o} Northwards and 0.17 ^{o} Eastwards, which is 23.5 km with an angle 58.7 ^{o} anticlockwise from the East direction. If this displacement is projected on the horizontal wave vector direction it is equal to 13 km, which is small compared to the 155 km total horizontal wavelength. Therefore, in this case the satellite profile can be considered vertical. In order to quantify the possible distortion of the vertical wavelength observed in the slanted SABER profile we use the formula derived by de la Torre et al. [2018]. According to the elevation angle of the sounding (23.1 ^{o}) and the orientation angle of the wave vector found when it is projected on the vertical plane defined by the retrieval (86.7^o), the possible error is about 12% (both angles are defined with respect to the ground). The GW intrinsic period was also calculated with our solution and the aid of the horizontal velocities provided by the ERA Interim reanalysis and was about 2.2 hours (19.6 m/s is the average speed parallel to the horizontal wavevector between the mountain tops around 600 mb where presumably the waves are generated and the maximum altitude of our study at approximately 3 mb). The aspect ratio (the division of vertical and horizontal scales) and intrinsic period of this wave belong to the hydrostatic non-rotating regime, close to the border with the non-hydrostatic spectral sector [Gill, 1982].

Notice that changing the choice of the initial pair (one profile from the lidars and one from SABER) leads from Eqs. (3) and (4) to a different 2x2 linear equation system to be solved but both are equivalent, which means that they lead to the same solution. We now evaluate the impact of uncertainties in the specified parameters of any of both equation sets, which are represented by a 2x2 M matrix (4 distances) and a column vector b (2 phase differences). The equation set is then represented by

$$Ms = b \tag{6}$$

and to evaluate if in our procedure any small changes in the known parameters can produce large changes in the solution s, we must calculate the condition number $K(M)$. Then [e.g., P. Alexander and de la Torre, 2010]

$$\epsilon_s \leqq \frac{K(M)}{1 - K(M)\epsilon_M}(\epsilon_M + \epsilon_b) \tag{7}$$

where ϵ_s, ϵ_M, and ϵ_b refer to the relative error of s, M and b respectively. $K = 1.47$ for any of both equivalent equation sets in our example (1 is the optimal value in any case). Distances can be given with high precision so their uncertainty can be estimated to be around 1 % ($\epsilon_M = 0.01$). Phase differences are extracted from the comparison of the same mode in the profiles at the two different places at the same time and we could evaluate them to be around 10 % ($\epsilon_b = 0.1$). Then, variations in the solutions would be around 15%. If the three profiles would become nearly collinear then the equation set would tend to an ill condition and the propagation of the precision errors to the solution would have dramatic effects through the increase of $K(M)$.

In general, it is possible to calculate the horizontal phase speed c_h, the horizontal and vertical components of phase velocity $c_{x,y,z}$ as seen from the ground for non-stationary waves

$$c_{x,y,z} = \frac{\omega}{k, l, m} \tag{8}$$

$$c_h = \mid \frac{\omega}{\sqrt{k^2 + l^2}} \mid \tag{9}$$

Figure 5 would exhibit tilted fronts for these waves and it would be clear if they are moving upwards or downwards. According to the signed outcome of Equations (3) and (4), if individual wavelengths and frequency have the same/opposite sign it must be interpreted as phase progression towards East/West and North/South. For intrinsic quantities ω has to

be replaced by $\hat{\omega}$. In our example:

$$\hat{c}_{x,y,z} = -19.6,\ -510,\ 0.6 \text{ m/s}$$
$$\hat{c}_h = 19.6 \text{ m/s}$$

Notice that due to the condition that the ground-based horizontal phase speed is zero, $\hat{c}_h$ becomes determined by the reanalysis wind speed component parallel to the horizontal wavevector used in the GW dispersion relation verification through Equation (5).

The GW associated specific potential energy can be also calculated over at least one wavelength as

$$E_p = \frac{1}{2}\left(\frac{g}{N}\right)^2\left(\frac{T_o}{\overline{T}}\right)^2 \tag{10}$$

whereas the specific horizontal MF components may be obtained by an expression valid in the mid-frequency range [e.g., Ern et al., 2004]

$$F_{x,y} = -\frac{\lambda_z}{\lambda_{x,y}}\frac{1}{2}\left(\frac{g}{N}\right)^2\left(\frac{T_o}{\overline{T}}\right)^2 \tag{11}$$

where g is gravity, λ refers to the wavelengths, N can be obtained from any lidar profile and finally T_o and $\overline{T}$ are the gravity wave temperature amplitude and the background atmospheric temperature (which can be obtained from either lidar) respectively. We obtain E_p = 44.6 J/kg, $F_x = -1.45$ J/kg and $F_y = -0.06$ J/kg. The average density in the studied height interval is 1.19 x 10^{-2} kg/m^3 and both components of momentum flux then respectively become -0.018 Pa and -0.001 Pa.

4 Conclusions

We have shown in a zone with high GW acvtivity through one illustrative example that it is possible to reconstruct the 3D structure of a dominant wave observed by two close simultaneous lidar soundings and an additional vertical temperature profile. The described method may help to dodge a present difficulty as is the determination of the 3 signed components of the wavevector. This is an essential quantity to determine directional MF, which is strongly related to atmospheric model parameterizations of GW drag. The last element is an Achilles heel that affects the simulation of zonal mean wind and temperature structure at mid- and high-latitudes. In particular, orographic waves like those generated in the hotspot here studied are currently considered to make significant contributions to the vertical transport of GW MF [e.g., McLandress et al., 2012].

Diverse tests verified if all instruments are likely observing the same GW and no important side-effects contaminate the analysis. Only 1 out of 17 cases provided concrete results. This should be attributed to the fact that in several cases the diverse instruments were observing different phenomena or GW were too weak or affected by other effects or underwent diffusion, absorption, unstable or non-linear behavior. It should be noted that in some previous studies it was assumed that much longer latitude, longitude and time intervals contained the same GW with no additional verification of coherency. McDonald [2012] evaluated as a function of horizontal separation and time difference the percentage of GPS radio occultation paired profiles that may be expected to contain the same GW. For example, his estimations were that approximately 30% of the pairs at 50-60S in the Southern Hemisphere separated by less than 250 km and by less than 15 min were seeing the same GW. It is clear that an improved version of the Rio Gallegos lidar and eventually the 24 hour operation of both instruments would lead to a substantial increase in the number of cases meeting the required conditions.

The assumptions of the method should be recalled to constrain its validity: one dominant GW is observed by both lidars and the additional sounding, GW and background are adequately separated by the digital filter and there are no further aliasing effects in the horizontal plane than those considered.

5 Appendix

In Figure 7 we may see the spectral power for both lidars as a function of θ and s for the case that failed to meet the final test in order to be considered a possible standing GW. In Figure 8 we see the corresponding temperature perturbation against time and height for both lidars. The time frame of the coincident data for both sources is from June 07, 2018 01:04 (UTC) to 08:30 on the same day. It may be seen that in Rio Grande an upper stationary front of maxima is clearly defined for only approximately the last 1/3 of the total time. In average there is a horizontally layered structure that spans for the whole observational time and the plot might through an initial visual inspection be interpreted as a stationary GW from bottom to top, but our procedure rejects that possibility through the polarization relation verification. This fact may be related to the irregular upper maxima wavefront mentioned above. The physical cause for this behavior is unclear within the limits of the present study.

References

Alexander, M. J., and Grimsdell, A. W. (2013), Seasonal cycle of orographic gravity wave occurrence above small islands in the Southern Hemisphere: Implications for effects on the general circulation, *J. Geophys. Res. Atmos.*, *118*, 11,589–11,599, doi:10.1002/2013JD020526.

Alexander, P. and de la Torre, A. (2010), A Method to Infer the Three Cartesian Wavelengths of a Mountain Wave from Three Soundings, *J. Appl. Meteor. Climatol.*, *49*, 2069–2074, doi:10.1175/2010JAMC2348.1.

Alexander, P., Luna, D., Llamedo, P., and de la Torre, A. (2010), A gravity waves study close to the Andes mountains in Patagonia and Antarctica with GPS radio occultation observations, *Ann. Geophys*, *28*, 587–595.

Alexander, P., de la Torre, A., Schmidt, T., Llamedo, P., and Hierro, R. (2015), Limb sounders tracking topographic gravity wave activity from the stratosphere to the ionosphere around midlatitude Andes, *J. Geophys. Res. Space Physics*, *120*, 9014–9022, doi:10.1002/2015JA021409.

Alexander, P., Schmidt, T., and de la Torre, A. (2018), A method to determine gravity wave net momentum flux, propagation direction, and ”real” wavelengths: A GPS radio occultations soundings case study, *Earth Space Sci.*, *5*, 222–230, doi:10.1002/2017EA000342.

Baines, P. G., *Topographic Effects in Stratified Fluids*, Cambridge Univ. Press, New York, 1995.

Butchart, N., Charlton-Perez, A.J. et al. (2011), Multimodel climate and variability of the stratosphere, *J. Geophys. Res.*, *116*, D05102, doi:10.1029/2010JD014995.

Chu, X., Zhao, J., Lu, X., Harvey, V. L., Jones, R. M., Becker, E., et al. (2018), Lidar observations of stratospheric gravity waves from 2011 to 2015 at McMurdo (77.84^{o}S, 166.69^{o}E), Antarctica: 2. Potential energy densities, lognormal distributions, and seasonal variations, *J. Geophys. Res. Atmos.*, *123*, 7910–7934, doi:10.1029/2017JD027386.

de la Cámara, A., F. Lott, V. Jewtoukoff, R. Plougonven, and A. Hertzog (2016), On the Gravity Wave Forcing during the Southern Stratospheric Final Warming in LMDZ, *J. Atmos. Sci.*, *73*, 3213–3226, doi:10.1175/JAS-D-15-0377.1.

de la Torre, A., Alexander, P., Schmidt, T., Llamedo, P., Hierro, R. (2018), On the distortions in calculated GW parameters during slanted atmospheric soundings, *Atmos. Meas. Tech.*, *11*, 1363–1375, doi:10.5194/amt-11-1363-2018.

de la Torre, A., Schmidt, T., and Wickert, J. (2006), A global analysis of wave potential energy in the lower stratosphere derived from 5 years of GPS radio occultation data with CHAMP, *Geophys. Res. Lett.*, *33*, L24809, doi:10.1029/2006GL027696.

Ehard, B., Kaifler, B., Kaifler, N., and Rapp, M. (2015), Evaluation of methods for gravity wave extraction from middle-atmospheric lidar temperature measurements, *Atmos. Meas. Tech.*, *8*, 4645–4655, doi:10.5194/amt-8-4645-2015.

Ern, M., Hoffmann, L., and Preusse, P. (2017), Directional gravity wave momentum fluxes in the stratosphere derived from high-resolution AIRS temperature data, *Geophys. Res. Lett.*, *44*, 475-485, doi:10.1002/2016GL072007.

Ern, M., Preusse, P., Alexander, M.J., and Warner, C.D. (2004), Absolute values of gravity wave momentum flux derived from satellite data, *J. Geophys. Res.*, *109*, D20103, doi:10.1029/2004JD004752.

Fritts, D.C. and J. Alexander (2003), Gravity wave dynamics and effects in the middle atmosphere, *Rev. Geophys.*, *41*, 1003, doi:10.1029/2001RG000106.

Fritts, D.C., R.B. Smith, M.J. Taylor, J.D. Doyle, S.D. Eckermann, A. Dörnbrack, M. Rapp et al. (2016), The Deep Propagating Gravity Wave Experiment (DEEPWAVE): An Airborne and Ground-Based Exploration of Gravity Wave Propagation and Effects from Their Sources throughout the Lower and Middle Atmosphere, *Bull. Amer. Meteor. Soc.*, *97*, 425–453, doi:10.1175/BAMS-D-14-00269.1.

Geller, M. A., Alexander, M. J., Love, P. T. et al. (2013), A comparison between gravity wave momentum fluxes in observations and climate models, *J. Climate*, *26*, 6383–6405, doi:/10.1175/JCLI-D-12-00545.1.

Gill, A.E. (1982), Atmosphere and Ocean Dynamics, Academic Press, New York.

Hindley, N.P., Wright, C.J., Smith, N.D., and Mitchell, N.J. (2015), The southern stratospheric gravity wave hot spot: individual waves and their momentum fluxes measured by COSMIC GPS-RO, *Atmos. Chem. Phys.*, *15*, 7797–7818, doi:10.5194/acp-15-7797-2015.

Hoffmann, L., X. Xue, and M. J. Alexander (2013), A global view of stratospheric gravity wave hotspots located withAtmospheric Infrared Sounder observations, *J. Geophys. Res. Atmos.*, *118*, 416–434, doi:10.1029/2012JD018658.

Hoffmann, L., Grimsdell, A. W., and Alexander, M. J. (2016), Stratospheric gravity waves at Southern Hemisphere orographic hotspots: 2003 –2014 AIRS/Aqua observations, *Atmos. Chem. Phys.*, *16*, 9381–9397, doi:10.5194/acp-16-9381-2016.

Kaifler, N., Kaifler, B., Ehard, B., Gisinger, S., Dörnbrack, A., Rapp, M., Kivi, R., Kozlovsky, A. (2017), Observational indications of downward-propagating gravity waves in middle atmosphere lidar data, *J. Atmos. Solar-Terr. Phys.*, *162*, 16–27, doi:10.1016/j.jastp.2017.03.003.

Kaifler, B., Lübken, F.-J., Höffner, J., Morris, R. J., and Viehl, T. P. (2015), Lidar observations of gravity wave activity in the middle atmosphere over Davis (69^oS, 78^oE), Antarctica, *J. Geophys. Res. Atmos.*, *120*, 4506–4521, doi:10.1002/2014JD022879.

Llamedo, P., Salvador, J., de la Torre, A., Quiroga, J., Alexander, P., Hierro, R., et al. (2019), 11 years of Rayleigh lidar observations of gravity wave activity above the southern tip of South America, *J. Geophys. Res. Atmos.*, *124*, 451–467, doi:10.1029/2018JD028673.

McDonald, A. J. (2012), Gravity wave occurrence statistics derived from paired COSMIC/FORMOSAT3 observations, *J. Geophys. Res.*, *117*, D15106, doi:10.1029/2011JD016715.

McLandress, C., Shepherd, T.G., Polavarapu, S. and Beagley, S.R. (2012), Is Missing Orographic Gravity Wave Drag near 60^oS the Cause of the Stratospheric Zonal Wind Biases in Chemistry–Climate Models?. *J. Atmos. Sci.*, *69*, 802–818, doi:10.1175/JAS-D-11-0159.1.

Mlynczak, M. G., Energetics of the mesosphere and lower thermosphere and the SABER experiment, *Adv. Space Res.*, *20*, 1177–1183, 1997.

Nash, E. R., Newman, P. A., Rosenfield, J. E., and Schoeberl, M. R. (1996), An objective determination of the polar vortex using Ertels potential vorticity, *J. Geophys. Res.*, *101*, 9471–9478, doi:10.1029/96JD00066.

Orfanidis, S. J (1996), Introduction to Signal Processing, Englewood Cliffs, NJ: Prentice Hall.

Park, J., H. Lühr, C. Lee, Y. H. et al., A climatology of medium-scale gravity wave activity in the midlatitude/low-latitude daytime upper thermosphere as observed by CHAMP, *J. Geophys. Res.*, *119*, 2187–2196, doi:10.1002/2013JA019705, 2014.

Rapp, M., Dörnbrack, A., and Kaifler, B. (2018), An intercomparison of stratospheric gravity wave potential energy densities from METOP GPS radio occultation measurements and ECMWF model data, *Atmos. Meas. Tech.*, *11*, 1031–1048, doi:10.5194/amt-11-1031-2018.

Sato, K., Watanabe, S., Kawatani, Y., Tomikawa, Y., Miyazaki, K., and Takahashi, M. (2009), On the origins of mesospheric gravity waves, *Geophys. Res. Lett.*, *36*, L19801, doi:10.1029/2009GL039908.

Schmidt, T., Alexander, P., and de la Torre, A. (2016), Stratospheric gravity wave momentum flux from radio occultations, *J. Geophys. Res. Atmos.*, *121*, 4443–4467, doi:10.1002/2015JD024135.

Torrence, C., and Compo, G.P. (1998), A practical guide to wavelet analysis, *Bull. Am. Meteorol. Soc.*, *79*, 61–78.

Wang, N. and Lu, C. (2010), Two-Dimensional Continuous Wavelet Analysis and Its Application to Meteorological Data, *J. Atmos. Oceanic Technol.*, *27*, 652–666, doi:10.1175/2009JTECHA1338.1.

Wright, C.J., Hindley, N.P., and Mitchell, N.J. (2016), Combining AIRS and MLS observations for three-dimensional gravity wave measurement, *Geophys. Res. Lett.*, *43*, 884–893, doi:10.1002/2015GL067233.

Wright, C. J. and Hindley, N. P. (2018), How well do stratospheric reanalyses reproduce high-resolution satellite temperature measurements?, *Atmos. Chem. Phys.*, *18*, 13703–13731, doi:10.5194/acp-18-13703-2018.

Zhao, J., Chu, X., Chen, C., Lu, X., Fong, W., Yu, Z., et al. (2017), Lidar observations of stratospheric gravity waves from 2011 to 2015 at McMurdo (77.84^{o}S, 166.69^{o}E), Antarctica: 1. Vertical wavelengths, periods, and frequency and vertical wavenumber spectra, *J. Geophys. Res. Atmos.*, *122*, 5041–5062, doi:10.1002/2016JD026368.

Acknowledgments

Manuscript prepared under grants CONICET PIP 2017-2019 11220170100067CO, ANPCYT PICTO-2016-0089 and ANPCYT PICT-2018-00653. P. Alexander, A. de la Torre, P. Llamedo and R. Hierro are members of CONICET. SABER profiles were downloaded from http://saber.gats-inc.com/ whereas ERA Interim data were obtained from apps.ecmwf.int/datasets.

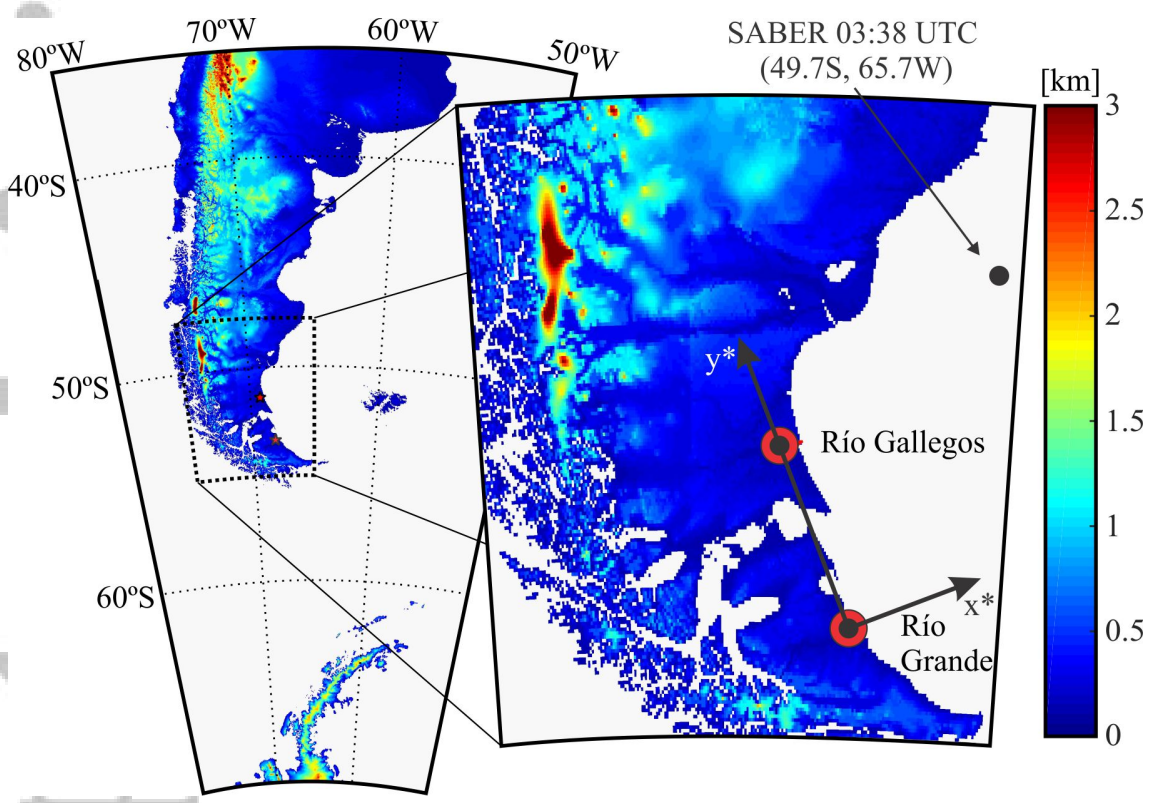

Figure 1. The location of the lidars in Río Grande and Río Gallegos and the topography of the region. The position of the SABER profile and the rotated horizontal axes $x*$, $y*$ are also shown.

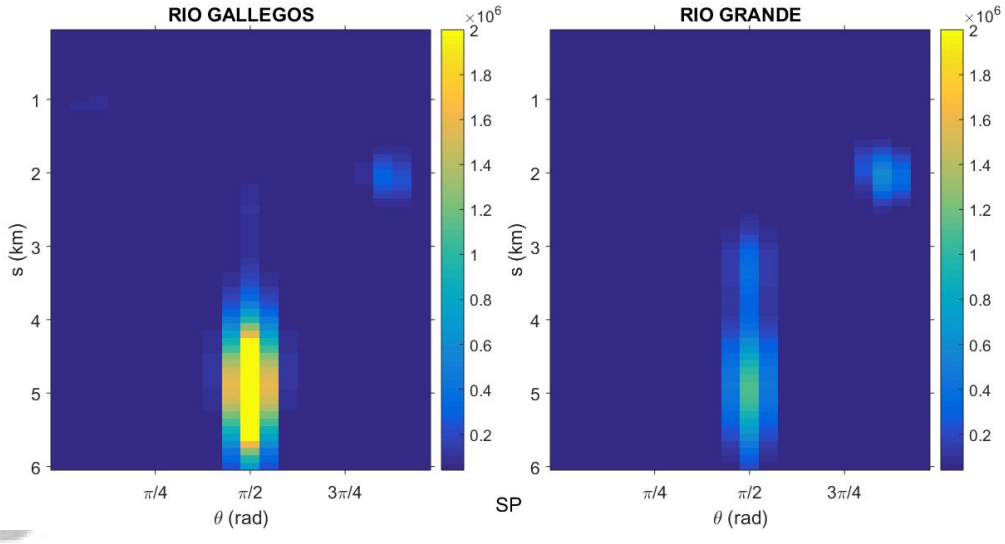

Figure 2. Spectral power for both lidars as a function of θ and s. For stationary wavefronts $\theta = \pi/2$ and s is equivalent to the vertical wavelength.

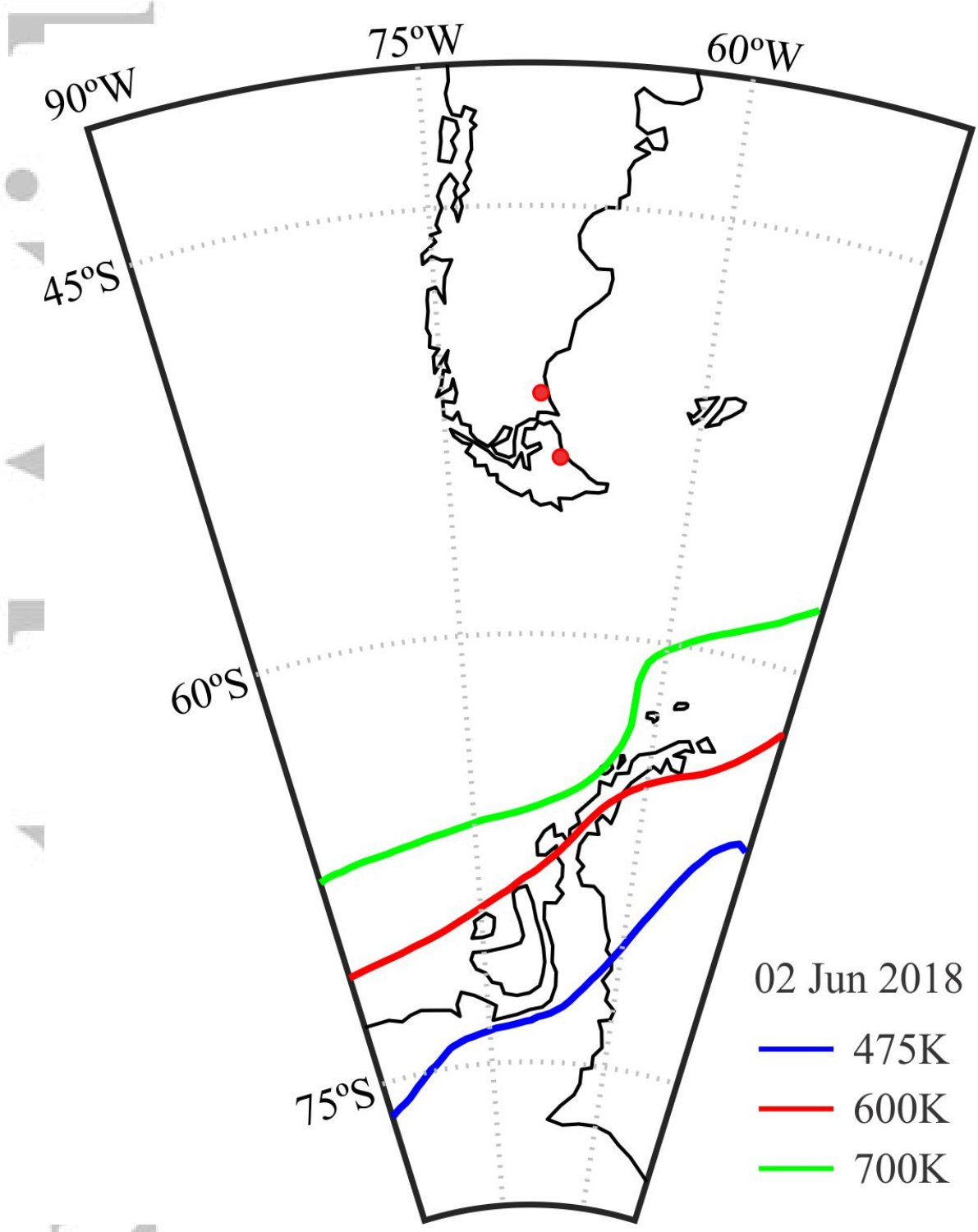

Figure 3. The vortex edge on June 02, 2018 00:00 UTC calculated for roughly 20, 24.5 and 28 km (blue, red and green) which correspond to the given isentropic levels.

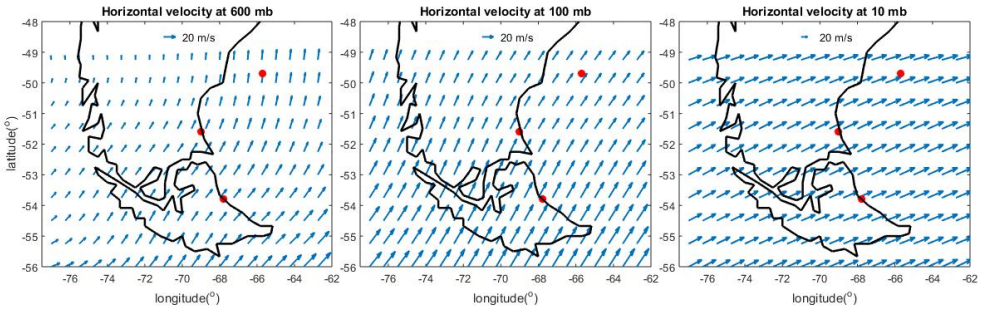

Figure 4. The horizontal wind according to ERA Interim data at three different levels on June 02, 2018 00:00 UTC. On top of each panel a standard arrow length is shown for magnitude reference.

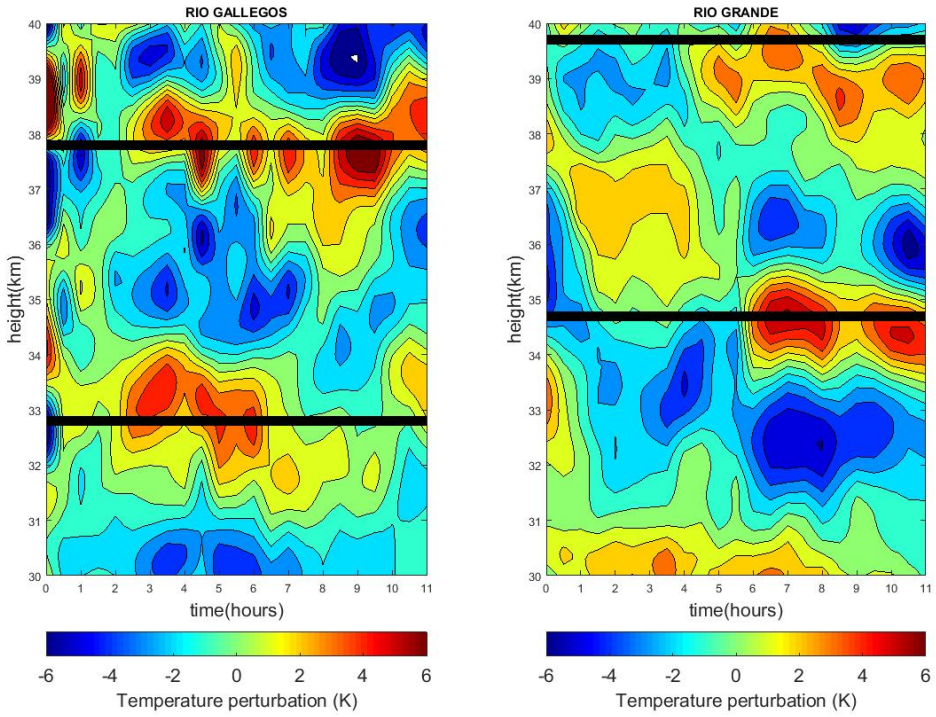

Figure 5. T' against time and height for both lidars, starting on 01-Jun-2018 22:35 UTC. Thick black lines represent best fit maxima for stationary wavefronts of 5 km vertical wavelength.

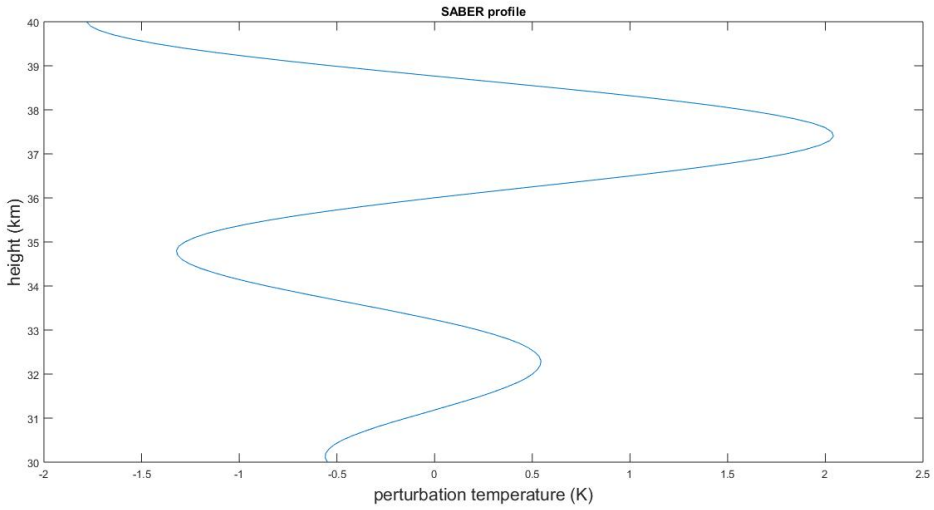

Figure 6. SABER temperature perturbation profile located 65.7W, 49.7S, 02/06/18 03:38 UTC in the 30 to 40 km height range.

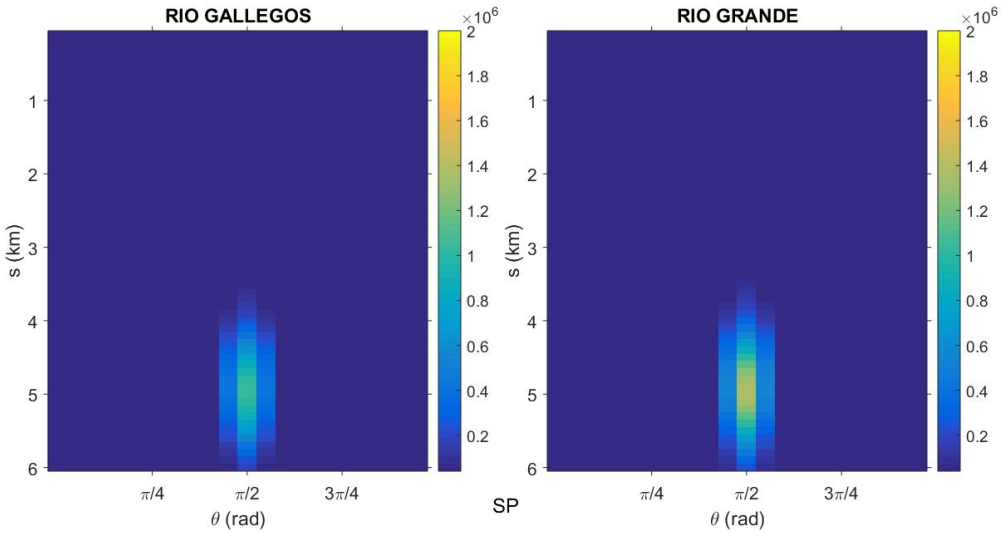

Figure 7. Spectral power for both lidars as a function of θ and s in the discarded case.

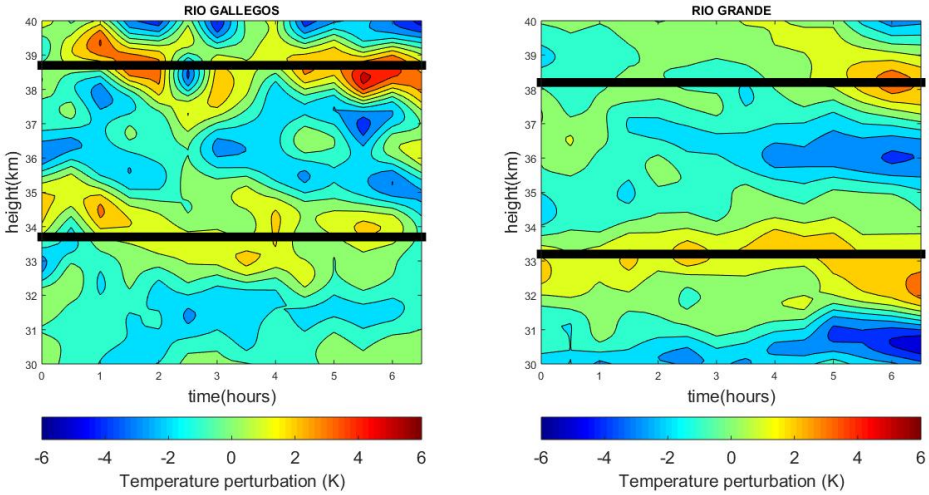

Figure 8. T' against time and height for both lidars in the discarded case, starting on 07-Jun-2018 01:19 UTC. Thick black lines represent best fit maxima for stationary wavefronts of 5 km vertical wavelength. If compared with Figure 5, it should be considered that the different aspect ratio is due to the fact that both cases do not have the same time extension.